Report no. changed (Mar 2006): SR-282-UU

NATO OTAN

Undersea Research Centre
Centre de Recherche Sous-Marine

Remote sensing of topographically-induced upwelling in the southern coastal region of Sicily

Farid Askari

NORTH ATLANTIC TREATY ORGANISATION ORGANIZATION DU TRAITE DE L'ATLANTIQUE NORD

September 1998 Report SR-282

SACLANTCEN SR-282

Remote sensing of topographically-induced upwelling in the southern coastal region of Sicily

Farid Askari

The content of this document pertains to work performed under Project 014-1 of the SACLANTCEN Programme of Work. The document has been approved for release by The Director, SACLANTCEN.

Jan L. Spoelstra
Director

intentionally blank page

Remote sensing of topographically-induced upwelling in the southern coastal region of Sicily

Farid Askari

Executive Summary:

In shallow littoral waters, upwelling can have profound impact on naval ASW and MW operations because it induces vertical as well as horizontal anomalies in the distributions of optical and acoustical properties. In addition to the wind-induced upwelling response produced at the coastal boundary, variations in bottom topography can generate upwelling. This report investigates the anomalous surface signals due to topographically-induced upwelling, which are detectable by different satellite sensors in terms of ocean temperature, colour, height and small-scale roughness fields. The concept of sensor fusion/synergism is demonstrated and a set of genetic indicators identified for the identification and tracking of upwelling using multiple fields. Remotely sensed surface signatures are also related to subsurface topography.

intentionally blank page

Remote sensing of topographically-induced upwelling in the southern coastal region of Sicily

Farid Askari

Abstract: Upwelling signatures caused by variations in bottom topography along the southeastern Sicilian coast are identified, using spaceborne remote sensing Advanced Very High Resolution Radiometer (AVHRR) imagery, ERS-1 and RADARSAT Synthetic Aperture Radar (SAR) imagery, Topex/Poseidon/ERS-2 (TPE) altimeter maps, and historical Coastal Zone Colour Scanner (CZCS) imagery. Topographically-induced upwelling appears to be a quasi-permanent feature along the southeastern coast of Sicily where sharp transitions occur in the bottom slopes. In AVHRR and historical CZCS imagery, upwelling signatures are manifested as 3 to 4 km wide bands of cold nutrient-rich waters running parallel to the shelfbreak. Collocated with the optical signatures, are step-type SAR modulations as well as bands of enhanced surface roughness the locations of which are coincident with topographic breaks in the bottom slope. On the downstream of the Malta Plateau is another prominent upwelling site which forms in concert with the arrival of the Malta eddy, mainly during late summer and early fall. While the formation of the eddy is largely dependent on the strength of density stratification, the bottom topography is the important triggering agent. The eddy rotates cyclonically which contributes to upwelling, reducing the SST by about 1 to 2 C^0 inside the eddy with respect to the ambient ocean. Historical CZCS imagery also show increases in pigment concentrations associated with the eddy. In TPE altimeter maps, the eddy is manifested as a 40 to 50 km wide "bowl-shaped" structure, with negative sea height anomalies ranging between 6 to 10 cm. The eddy-type motion is further evidenced in SAR imagery by the appearance of striations forming within the center and the boundaries of the eddy. The study demonstrates the utility of sensor fusion and identifies a set of genetic indicators for upwelling identification and tracking using multiple sensors.

Keywords: bottom topography, upwelling, SAR, AVHRR, altimeter, sensor fusion.

Contents

1 Introduction

Divergence in horizontal flow causing depletion of water in the surface layer, leads to upwelling or ascending motion, replenishing the surface layer with water from below. It is estimated that about half of the world's fish supply is produced in upwelling regions (Ryther, 1969). Upwelling also has profound influence on the optical and acoustical properties of the sea. Upwelling regions generally have higher concentrations of phytoplankton which tend to absorb blue light and reflect green light, hence they appear greener than the ambient waters. The increased level of biological activity can also result in higher levels of ambient acoustic noise. The spatial inhomogeneities in the temperature field also introduce changes in the index of refraction, hence the sound speed, which in turn alters the pattern of acoustic propagation and energy distribution. Additionally, upwelling regions are characterized by high levels of suspended particulate matter, which can lead to significant sound attenuation at high acoustic frequencies (Richards *et al*., 1997).

Wind-induced-coastal and equatorial upwelling are two classical types of upwelling the dynamics of which have been studied extensively (Smith, 1968). Away from coastal boundaries, several other mechanisms including variations in bottom topography, meandering currents, and current-bottom-interactions can induce upwelling on the continental shelf. Hsueh and Ou (1975) show that shelfbreak upwelling can be generated by the "β-effect", due to the latitudinal variations of Coriolis parameter, acting on a steady current flowing along the shelfbreak. Also on a β-plane, Hill and Johnson (1974) show that in the presence of a steady wind and constant density, upwelling can be produced at the shelfbreak when the circulation of the continental shelf is joined with the deep ocean through a shear layer. Janowitz and Pietrafesa (1980) show that for time-dependent winds on an f-plane (constant Coriolis parameter), domes of upwelling form directly over the shelf break. Janowitz and Pietrafesa (1982) and Pietrafesa (1983) show that upwelling is generated when the bottom isobaths separate or diverge in the downstream direction of a sheared longshore current. Topographic bottom anomalies also generate deflections and meanders in geophysical fluid flows, as the fluid seeks to conserve potential vorticity in response to changes in its vertical thickness. Differential lowering of the sea surface conducive to upwelling is associated with turning processes (Chew, 1974).

One of the most promising means of acquiring synoptic information on upwelling is by satellite remote sensing. The primary ocean surface parameters detectable by

satellite remote sensing are temperature, colour, roughness and slope (or sea height). The goal of this paper is to identify through the synergy of different sensor outputs, the anomalous surface signals due to upwelling processes which become detectable in more than one parameter. For detecting upwelling signatures, previous studies (McClain *et al.* 1984) have relied on passive sensors (thermal infrared and visible scanning radiometers) using low sea surface temperature anomalies, or high photosynthetic pigment concentrations as indicators. In this study we construct a more expanded view of upwelling processes along the southern coast of Sicily. By combining the traditional optical passive-sensors which measure properties of the water with active sensors (altimeter and SAR), we show the influence of upwelling on the surface properties such as the roughness and height fields. A key aspect of this study is the fusion of multi-parameter information and the coupling of water properties to the surface properties through dynamical coupling.

The organization of the report is as follows. Section 2 describes the details of the experiment including the region's bathymetry, general circulation, and types of sensors used in the study. Section 3 includes results and discussion. Using an assortment of satellite observations, *in situ* measurements, simulation results, and historical findings we examine the remotely-sensed surface signatures of upwelling processes. Three mechanisms, including topographically-induced, meander-induced and wind-induced-coastal upwelling are identified. Section 4 contains the conclusions. The study demonstrates the utility of sensor fusion and identifies a set of generic indicators for upwelling identification and tracking using multiple sensors.

2
Experimental methods and setting

The present study involves the analysis of oceanographic and remote sensing measurements collected during the NATO Rapid Response 96 (RR96) experiment August to October 1996. The study area covers the southwestern coast of Sicily (Fig. 1). The shipboard oceanographic measurements for the exercise included acoustic Doppler current profilers (ADCP), conductivity-temperature-depth (CTD), and expendable bathythermographs (XBT) measurements. The spaceborne remote sensing data used in this study consisted of AVHRR imagery from the NOAA satellites, SAR imagery from the ERS-2 and RADARSAT satellites, the TPE altimeter sea height anomaly maps, and the historical CZCS imagery from the NIMBUS-7 satellite.

The Defence Evaluation and Research Agency (UK), the Defence Research Establishment Atlantic (Canada,) Naval Oceanographic office (US), and the SACLANT Centre provided remote sensing imagery in near-real-time. Harvard University provided oceanographic modeling results utilizing the Harvard Ocean Prediction System (HOPS). The HOPS simulation results (Robinson, 1998) are used to corroborate the satellite remote sensing measurements.

2.1 BATHYMETRY AND GENERAL CIRCULATION

Because many of the remotely sensed surface signatures described in subsequent sections appear to be dynamically linked to the underlying bathymetry, some of the details are described here. The southern Sicilian continental margin extending from Cape Granitola and Cape Passero can be divided into three morphological regions (Fig. 2): the northwest region containing Adventure Bank, the central region extending from Cape Granitola to Punta Secca, and the southeast region containing the Malta Plateau. The Adventure Bank is the dominant topographic feature in the northwest region having a wide shelf that extends 40 to 50 km offshore. In the central region, a series of cuspate bays form the coastline. In this region, the shelf is only 5 to 7 km wide and the 200 m isobath generally runs parallel to the coast. To the south of Punta Secca, the shelf widens. The 200 m isobath veers south, around the island of Malta turning north, forming the southeastern shelf region, or the Malta Plateau. On the Malta Plateau itself, due south of Capo Passero, is a rock outcrop known as Ragusa Ridge. To the west of the ridge lies a U-shaped sedimentary basin which separates the islands of Malta

and Sicily. Along the rim of the basin, sharp slope transitions occur between the 50 and 100 m isobaths (Figure 2).

The near surface circulation in the Strait of Sicily is dominated by the eastward flowing Atlantic Ionian Stream (AIS), which couples the surface circulation of the eastern and western Mediterranean. Hydrodynamic instabilities associated with this current, occuring in the form of meanders and eddy-like features, are causally related to interactions of the currents with the bottom. These circulatory features are modulated by wind-forced Rossby waves (Pierini, 1996), and wind-driven coastal currents. The details of ocean circulation and variability within the Sicily Strait are described by Manzella *et al.* (1990), Tziperman and Malanotte-Rizzoli (1991), Moretti *et al.* (1993), Roussenov *et al.* (1995), Onken and Sellschopp (1998).

2.2 REMOTE SENSING DATA

During the RR96 experiment, AVHRR imagery was down-linked in real-time using the SeaSpace TeraScan high resolution picture transmission system at SACLANTCEN. The images were geometrically rectified and calibrated for sea surface temperature (SST) analysis. The image analysis involved identification of fronts, eddies, filaments and patches with anomalous SST distributions. The digital coordinates of the features were transferred to a geographic information system for subsequent merging with other satellite data.

The only source of ocean color data for our region was the historical CZCS imagery acquired by the NIMBUS-7 satellite during the period 1978-1986. The CZCS sensor carried five visible channels and one infrared channel. The bands were chosen to respond to the known properties of chlorophyll absorption. For a review of bio-optical algorithms which rely on spectral radiance ratios for deriving pigment concentrations and total suspended sediments the reader is referred to Gordon and Clark (1980), and Morel (1980). The CZCS images for this study were obtained from the NASA Goddard Distributed Active Archive Center. Here we focus on detecting relative changes in chlorophyll concentrations, and correlating the spatial relationships between the biologically productive regions and the positions of the thermal fronts and topographic anomalies.

The surface roughness fields were derived from the C-band SAR (5.3 GHz, wavelength: 5.7 cm) instruments flying on board the ERS-2 and RADARSAT satellites. The ERS-2 SAR uses vertical polarization for transmission and reception (VV) and has a fixed incidence angle (23^{o}), whereas RADARSAT uses horizontal polarization for transmission and reception (HH). The RADARSAT antenna is also configured with an electronic beam steering mechanism which

allows for changing incidence angles between 20° and 60°. At C-band, the slope (Alpers and Brummer, 1994) of the wind scatterometer model function is 1.1 (for 23° incidence, VV polarization), making the Bragg-scale waves highly sensitive to the wind. The SAR directly maps the spatial distribution of Bragg-scale waves which may be modulated by longer gravity waves, variable wind stress, changes in the atmospheric thermal stratification, surface films, and variable surface currents. Here we identify changes in small-scale roughness associated with thermal and velocity fronts, surface films, internal waves and other process related to upwelling. Additionally, we utilize the SAR as a high-resolution imaging scatterometer, deriving the spatial variations of the wind vector. With absolute calibration, the SAR image intensity can be related to the normalized radar cross-section, and hence to the wind speed *via* a model function. However, as SAR responds only to the line-of sight component of the wind vector, the true wind direction must be measured independently, or derived from image processing techniques utilizing physically recognizable patterns such as wind-waves, wind-streaks and roll vortices.

The combination of TPE altimeter data are used to derive sea height anomaly maps which show dynamic heights of ocean features such as fronts and eddies relative to a static geoid or a mean sea level (in this case the JGM-3 gravity model). Archival data pertinent to the study were obtained from the world-wide-web home-pages maintained by the University of Colorado. The anomaly maps are constructed using altimeter passes over one complete 35-day cycle of ERS-2, with TOPEX providing additional coverage every 10 days. The environmental corrections including inverted barometer, wet and dry troposphere, ionosphere, e-m bias, and tides are applied to the individual passes prior to constructing the maps. For the region of interest extending between 12° to16° E and 35° to 38° N, a sea height anomaly map is constructed utilizing a nearest neighbor surface interpolation scheme using 13 passes from ERS-2 and 15 passes from TOPEX.

3
Results and Discussion

Here we investigate the remote sensing signatures for three types of upwelling: topographically-induced, meander-induced, and wind-induced-coastal upwelling using the traditional optical sensors (AVHRR and CZCS) in concert with the active SAR and altimeter sensors. The relationship between anomalous surface signals in the roughness, temperature, color and height fields with bottom topography is discussed.

3.1 TOPOGRAPHICALLY-INDUCED UPWELLING

We focus the discussions here on a recurring roughness which appears to the south of Punta Secca, extending to the southeast in some SAR images taken during the RR96 experiment. Figure 3 is a C-band (VV) ERS-2/SAR image taken on 21:20 UT on 9 September. The roughness front is characterized in the central portion of the image by a step-type change in radar backscatter, with modulations increasing to the southwest side. The contrast across the front, becomes less pronounced, moving to the southeast and northwest corners. It is evident from the AVHRR image taken at 2:14 UT on the same day that the roughness front is associated with a narrow curved cold filament which extends diagonally from northwest to southeast (Fig. 4). Inside the filament which is wide at its two extremities (4 to 5 km) and narrow in the center (1 to 2 km), the SST decreases by about 1^{o} to 2^{o} C. The location of the fronts illustrates the spatial relationships between the roughness and IR fields.

The AVHRR image (Fig. 5) taken on the previous day, indicates that the filament was slightly wider, and its main axis was 2 to 3 km further to the south. The corresponding RADARSAT SAR image (Fig. 6) which is also C-band, but HH-polarized, shows less prominent roughness variations associated with the cold filament. A trough-like low backscatter region, compared to the one-sided step of the VV case, extends from about 14.8^{o} E and 36.6^{o} N to about 15.12^{o}E and 36.4^{o}N. Along the northern boundaries, step-type modulations appear, but they are much weaker than the VV-polarized signal. Also, the filament's southern boundaries are less distinct with modulation gradually increasing to the southwest.

A CZCS image acquired on 15 September, 1983 is shown in Fig. 7. There are indications of narrow bands of high surface chlorophyll concentrations along the coast. At about 14.5°E the bands separate from the coast and extend to the southeast, forming plume-like features several km wide. As chlorophyll has an absorption peak near 440 nm, as the chlorophyll concentration increases, it suppresses the blue portion of the spectrum in turn making the upwelling bands look more green.

Several images illustrate a clustering of frontal structures within a narrow band extending southeast from offshore of Punta Secca to the west of Ragusa Ridge (15.1°E). Superimposing the spatial distributions of the roughness, IR, and color fronts on the detailed bathymetric map (Fig. 8) indicates that the fronts are confined to a region between 50 and 100 m isobaths where sharp changes in bottom slope occur. The close association between the frontal positions and changes in the bottom leave little doubt that some form of topographic steering or trapping occurs. Previous theoretical studies (Janowitz and Pietrafesa 1980) show that upwelling domes are expected to form over the topographic breaks in shelf regions where bottom slopes and curvatures undergo abrupt shape changes, when the quantity $h(h_{xx})/2(h^2)_x$ is greater than unity; where h is the water depth, x is the offshore spatial coordinate, h_x is the diabathic bottom slope and h_{xx} is the rate of change of slope. In this case h_x changes from 10^{-3} to10^{-2} and h_{xx} is $1.8\text{x}10^{-5}$ m^{-1}. Thus we suggest that the thin-cold filaments observed in AVHRR imagery are surface signatures of upwelling bands forming along the topographic breaks.

As noted above, coexisting with the thin-cold filaments are anomalous surface signals in the roughness field. The upwelling-induced roughness front becomes visible in SAR imagery as a consequence of the wind stress variability near the SST front. As colder water is transported to the surface, the distribution of atmospheric stratification (Askari *et al.,* 1993) is changed near the front, causing variations in wind stress and hence radar backscatter. Comparing the modulation signatures for HH to VV polarized images indicates a polarization dependence in the thermal-stability imaging mechanism. The VV signals exhibit the typical step-like modulations, while the HH signals showed much weaker signatures. Additional studies are needed to conclusively demonstrate this dependence, as the HH and VV images were not taken simultaneously.

Several other noteworthy features appear in the RADARSAT image (Fig 6). An internal wave packet appears at around 15.05°E, and another group appears further east at around 15.125°E. The locations of the packets are coincident with the western and eastern flanks of the Ragusa ridge where the shelf topography suddenly descends on both sides. Tidal forcing is suspected to be the cause of their generation mechanism.

There is evidence of bright, narrow backscattering bands, off the southern tip of Sicily. The processes contributing to the formation of bright, narrow bands have been attributed to wave current interactions and small-scale wave-breaking along convergence fronts (Lyzenga 1991). In our case, the IR field shows a correspondence between the bright roughness bands and weak SST fronts forming at the confluence of warmer waters from the north and cooler waters to the west.

3.2 MEANDER-INDUCED UPWELLING

In the preceding section we discussed upwelling processes caused by local topographic anomalies on the Malta Plateau, due to the horizontal and vertical dimensions of which, the Malta Plateau is a prominent topographic obstacle for geophysical fluids with comparable length scales. The domain of influence extends several km downstream and to the east, invoking changes in circulation, temperature, color, sea surface height, and roughness fields.

We begin with the interpretation of the SAR image (Fig. 9) taken on 28 August over a region to the east of the tip of Sicily. The image shows a series of curvilinear striations with changing orientations, centered at 15.33°E, 36.63°N. The striations are embedded in a region of reduced backscatter, which increases in intensity moving away from the center. In SAR imagery, there are at least two phenomena which can give rise to bright-dark striations patterns. The first is caused by short gravity waves/current interactions along shear fronts and eddies (Cheney, 1981), the second by the interaction of waves with internal wave-induced current (Alpers, 1985). In both cases, the mechanism responsible for SAR imaging., is the straining of the short scattering waves by the gradients in surface currents. Given the historical evidence for the persistence of eddy-like circulations at this location during the summer and early fall (Onken and Sellschopp, 1998), we attribute the striation signatures to eddy-induced wave-current interactions effects. There is also persuasive evidence that as a consequence of eddy like circulation, in addition to changes in currents and surface roughness, other processes including SST, color, and the sea height distributions also change.

It is a well known phenomenon that cyclonically rotating eddies induce upwelling. We have documented the appearance of isolated oval/circular-shaped cold water patches in the AVHRR images from 28 August, and 8 and 9 September. Superimposing the SST frontal locations on the SAR image (Fig. 9) again shows a correspondence between the cold pools located at the eddy center and the area of reduced roughness. Furthermore, we have independent evidence (Fig. 10) from the HOPS model simulations (Robinson *et al.,* 1998) for the existence of cyclonically rotating currents as well as well as patches of cooler water (by 1° to 2°C) at 37°N, 13°E and 36.7°N, 15.5°E. Inside eddies, upwelling

results from the continuous supply of positive vorticity, which has a pump-like effect bringing cold interior waters to the surface.

A first-order estimate for the upwelling velocities can be obtained from the surface parameters in conjunction with the conservation of potential vorticity (Arthur, 1965)

$$f\frac{dw}{dz} = \frac{d\xi}{dt} + \beta v \tag{1}$$

where w is the vertical velocity, z is the depth, f is the Coriolis parameter, β is the change in planetary vorticity with latitude (1.35×10^{-13} $cm^{-1}s^{-1}$), and v is the tangential velocity and $\xi = \frac{v}{r} - \frac{\partial v}{\partial r}$ is the vertical component of relative vorticity expressed in polar coordinates with r being the radial distance. Integrating Eq. (1) from some depth (h) to the surface we obtain the vertical velocity

$$w = -\frac{h}{f}\frac{d\xi}{dt} - \frac{h\beta v}{f} \tag{2}$$

For vortex-like circulation, we can express the balance of forces in the radial direction as

$$\frac{v^2}{r} + fv = \frac{1}{\rho_o}\frac{\partial p}{\partial r} = fv_g \tag{3}$$

where p and ρ_o are pressure and density, respectively. Solving the quadratic equation for the tangential velocity v

$$v = -\frac{fr}{2} + \left[\frac{f^2r^2}{4} + frv_g\right]^{1/2} \tag{4}$$

Where (v_g) is the geostrophic current which is driven by the sea level tilts

$$v_g = \frac{g}{f}\frac{\partial \eta}{\partial r} \tag{5}$$

where g is the acceleration due to gravity, and η is the surface height. Now, we can derive the sea surface height and slopes in (5) from satellite TPE altimeter

measurements, which show (Fig. 11) evidence of "bowl-shaped" troughs with sea height anomalies of -10 to –12 cm forming, in the lees of the Adventure Bank and the Malta Plateau, at 37.4° N, 13.3° E and at 36.7° N, 15.4° E. On the ocean surface, the trough corresponds to a differential lowering or tilting of the sea surface within the turning region, analogous to the inward inclination of the roadbed in a curving speedway (Chew, 1974). The troughs are common occurrences within the meander-deflection regions, when oceanic and atmospheric currents flow over topographic anomalies (Rooney and Janowitz, 1979).

Taking η = 10 cm, r = 25 km (from AVHRR imagery) for the Malta eddy with f =8.85×10^{-5} s^{-1}, and v_g = 44 cms^{-1}, we arrive at a tangential current (v) of 37 cms^{-1}, which is consistent with the shipboard ADCP measurements taken three weeks earlier at the same location (Fig. 12). Using the above values in (2) with h = 50m, $\beta = 1.35\times10^{-13}$ $cm^{-1}s^{-1}$, $d\xi/dt = 2.25\times10^{-10}$, we finally arrive at an estimate for the vertical velocity which is on the order of $1.3x10^{-2}$ cms^{-1}. One of the consequences of vertical motion is the uplifting of isotherms in the core of the eddy which produces a dome-like (an upward and downward bending) density structure. As shown in Fig. 13, in crossing the eddy's boundaries, the vertical spacing of isopycnals changes by a factor of 4. As noted in the introduction, these spatial inhomogeneities can introduce significant changes in acoustic propagation and energy distributions. The above calculations show how the remotely-sensed surface parameters can be utilized to arrive at first order estimates of the vertical structure. From the standpoint of observable surface parameters, we expect to find larger amplitude meanders, larger sea height anomalies, hence enhanced upwelling velocities during summer and early fall when stratification is strong. Strong stratification tends to restrict vertical motion over the bottom, forcing the flow to pass around, instead of over an obstacle.

3.3 WIND-INDUCED COASTAL UPWELLING

On the SAR imagery (both VV and HH-polarized) of the coastal regions, we have noticed the appearance of several dark patches (low radar reflectivity) immediately adjacent to the coastal embayments (Fig. 3 and 6). The accompanying AVHRR imagery (Fig. 4,5) suggests that the dark patches are coincident with cold water pockets where SSTs are reduced by 1 to 2°C. As with the dark roughness patches, the cold pockets are highly irregular, extending several km offshore in some places and only 2 to 3 km in others. Piccioni *et al*. (1988) attribute the cold SST pockets in this region to wind-induced upwelling, which emerges about three days after the onset of an east southeast alongshore wind. During late summer and early fall, alongshore winds are predominantly westerly and northwesterly (Roussenov *et al.* (1995). Therefore, it is probable that

dark radar patches appearing adjacent to the coast are linked to wind-induced upwelling. However, we cannot exclude the possibility of other mechanisms, such as coastal wind-sheltering or damping of Bragg waves by surface film. With regard to the patchiness of the upwelling signal, several mechanisms can cause this. As shown by Askari, *et al.* (1989), longshore variations in coastline geometry can introduce spatial gradients in the wind and height fields, which in turn give rise to asymmetrical distributions of mass balance normal to the coast. The presence of small capes can also give rise to vortex type circulation for winds normal to a coast, and source/sink points for winds parallel to the coast (Saint-Guily, 1982). Also as discussed by Cushman-Roisin (1994), a local upwelling source can send a wave signal along the coast in the form of an internal Kelvin wave, decreasing the rate of upwelling in forced region, while increasing upwelling in the unforced regions.

Upwelling can also influence the coastal sea level distribution via the steric effect. Through this effect, sea levels within upwelling zones can drop relative to the surrounding warmer waters because of cooling and thermal contraction. The steric signal contribution to the mean sea level variations in the Mediterranean as measured by altimetry is of the order of 10 cm (Larnicol *et al.* 1995). The magnitudes of the expected signals at the coast can be expressed by the sea level slope at the coastal boundary (Askari, *et al.,* 1989, Eq. 15)

$$\frac{gh\rho}{\rho_0 f}\left(\frac{\partial \eta}{\partial x} A\right) = -\frac{1}{f}(\tau^y E) - \frac{gh^2}{\rho f}\left(\frac{\partial \rho}{\partial x} D\right) \qquad (6)$$

where the left hand side describes the slope, the first term on the right is due to wind forcing, and the second term is thermohaline forcing. The A, D, and E coefficients are functions of the Ekman depth, $\delta_E = (2A_v/f)^{1/2}$ and h is the water depth. Now for $h/\delta_E >> 1$, $A \sim \delta_E$, $D \sim 1$ and $E \sim -1$ (see Askari *et al.,* 1989). The first term on the right hand shows how an alongshore (upwelling favorable) wind can lower the sea level at the coast, *via* the offshore Ekman drift by transporting water away from the coastal boundary. And the second term shows how the tilting of the isopycnals can contribute to sea level tilts.

Using the remote sensing measurements of sea slope ($\frac{\partial \eta}{\partial x}$ from altimetry) and SAR-derived wind speeds (τ^y) in (6) the steric contribution ($\frac{\partial \rho}{\partial x}$) to the sea slope can be estimated. The wind vector magnitude can be estimated using the SAR image and the procedure described by Wackerman *et al.* (1996). The procedure is explained as follows. On the SAR image a group of 5×5 km cells are selected for analysis. The mean image intensities within each cell are computed and converted

to absolute radar cross-sections using radiometric calibration constants. The wind direction is estimated using the two-dimensional directional wave spectra within the 5×5 km cell. The CMOD4 scatterometer algorithm (Stoffelen and Anderson, 1993) is used to predict the wind vector, given the incidence angle, wind azimuth angle and the normalized radar-cross section:

$$\sigma_0 = b_0(1 + b_1 \cos\phi + b_3 \tan h\, b_2 \cos 2\phi)^{1.6} \quad (7)$$

where σ_0 is the normalized cross-section, ϕ is the wind azimuth angle, and b_0, b_1, b_2, and b_3 are functions of incidence angle and wind speed.

Now using h = 9 m (water depth) at the coast, and the altimetric measurements of diabathic sea slopes ($\partial\eta/\partial x$ of -1×10^{-6}), and τ^y = 1 dyncm^{-2} (equivalent to 5 ms^{-1}) from SAR-scatterometry, we obtain a first-order estimate of the slope of the thermohaline field $\partial\rho/\partial x = -0.7 \times10^{-6}$(0.7 cm over 10 km). This is a crude estimate of the steric signal, and unfortunately no direct measurement exists from the survey with which to validate the results. The proposed method provides an approach for combining remotely sensed measurements with dynamical models to assess the subsurface structure. In order to validate and separate the contributions of wind from thermohaline forcing, however, the altimeter measurements must be acquired simultaneously with field observations.

The appearance of upwelling signatures in historical CZCS imagery taken fifteen years ago is the most definitive proof that upwelling along the topographically-induced and eddy-forced upwelling are persistent and recurring phenomenon in this region. While upwelling signals are easily recognizable in terms of the water properties, i.e., the thermal and color anomalies, to ascertain correspondence with roughness which is a surface property, is more difficult. Another difficulty arises from the life cycles of the fields. Compared to the temperature and color, the roughness signatures are of shorter duration. The life-cycles of the temperature and color parameters are governed by diffusive and advective time-scales which are of the order of several minutes (or hours), while, for the Bragg resonance waves, the life-cycles are governed by the growth rate $\beta = 0.04\,(u^*/c)^2\,\omega$ (or $1/\beta$ = relaxation) (Plant, 1982) which is a function of the square of the wind speed (or friction velocity), where u^* is the friction velocity, c is the phase speeds, and ω is the wave frequency. For example for a C-band SAR the growth rates for Bragg-scale waves are $\beta = 0.20$ s^{-1} and 0.5 s^{-1} respectively for wind speeds of 3 ms^{-1} and 5 ms^{-1}. This shows that C-band scale waves tend to be especially responsive to the wind speed but less responsive to the effects of perturbing forces. Thus upwelling regions maintain their temperature, color, and sea level signatures, but not roughness signatures due to sudden changes in wind speeds.

4
Conclusions

Upwelling processes are complex phenomena involving interactions between winds, waves, currents, coastal boundaries, and bottom topography. Using a synergistic, remote sensing approach, in conjunction with field observations and theory we have studied upwelling processes which produce anomalous signals in the temperature, colour, height, and roughness fields. Upwelling regions can be characterized in terms of low SST, high pigment, and lowered sea levels relative to the ambient ocean. Among the remotely sensed signatures, the association of upwelling with roughness is the least understood. For SAR (VV-polarized) imaging, with the exception of thermally-induced wind-stress variations, which is a widely accepted mechanism for the imaging of thermal fronts, the precise nature of other mechanisms still eludes us. Additional verification is required for measuring wind-induced and thermohaline-induced slopes from altimetry near coastal boundaries.

Acknowledgments

The author thanks the following people and institutions for support to this study: Jane Flatman of DERA/UK for providing the ERS-2/SAR imagery (Fig. 4), Erick Malaret of ACT Corporation for assisting with the image processing, Jurgen Sellschopp and Gisella Baldasserini of SACLANTCEN for sharing the CTD and ADCP measurements from the RR-96 cruise, Alan Robinson of Harvard University for providing the HOPS simulation results, and Elvio Nacini of SACLANTCEN for help with the AVHRR image acquisition.

References

Alpers, W. (1985) Theory of radar imaging of internal waves. *Nature*. **314**, 245-247.

Alpers, W. and B. Brummer (1994) Atmospheric boundary layer rolls observed by the synthetic aperture radar aboard the ERS-1 satellite. *J. of Geophysical Research,* **99**, 12613-12621.

Arthur, R.S. (1965) On the calculation of vertical motion in eastern boundary currents from determinations of horizontal motion. *J. of Geophysical Research*, **70**(12), 2799-2803.

Askari, F., Pietrafesa, L.J., Janowitz, G.S. (1989) Steady, three-dimensional circulation on a cuspate continental shelf. *Continental Shelf Research*, **9**, 497-526.

Askari F., Geernaert, G.L., Keller, W.C., Raman, S. (1993) Radar imaging of thermal fronts, *International Journal of Remote Sensing*, **14**, 275-294.

Cheney, R.E. (1981) A search for cold water rings. *In spaceborne synthetic aperture radar for oceanography*, edited by R.C. Beal, P.S. DeLeonibus and I. Katz (Baltimore, London: The Johns Hopkins University Press), 161-170.

Chew, F. (1974) The turning process in meandering currents: A case study. *Journal of Physical Oceanography,* **4**, 27-57.

Cushman-Roisin, B. (1994) Introduction to geophysical fluid dynamics. Englewood Cliffs, NJ Prentice-Hall.

Gordon, H.R., Clark, D.K. (1980) Atmospheric effects in the remote sensing of phytoplankton pigments. *Boundary Layer Meteorology,* **18**, 299-313.

Hill, R.B., Johnson, J.A. (1974) A theory of Upwelling over the shelf break. *Journal of Physical Oceanography*, **4**, 19-26.

Hsueh, Y., Ou, H.W. (1975) On the possibilities of coastal, mid-shelf, and shelf break upwelling. *Journal of Physical Oceanography*, **5**, 670-682.

Janowitz, G.S., Pietrafesa, L.J. (1980) A model and observations of time-dependent upwelling over the mid-shelf and slope. *Journal of Physical Oceanography,* **10**, 1574-1583.

Janowitz, G.S., Pietrafesa, L.J. (1982) The effects of alongshore variations in bottom topography on a boundary current, or, topographically induced upwelling. *Continental Shelf Research*, **1**, 123-141.

Larnicol, G., Traon, P.L., Ayoub, N., De Mey, P. (1995) Mean sea level and surface circulation variability of the Mediterranean sea from 2 years of TOPEX/POSEIDON altimetry. *Journal of Geophysical Research,* **100**, 25163-25177.

Lyzenga, D.R. (1991) Interaction of short surface and electromagnetic waves with ocean fronts, *Journal of Geophysical Research,* **96,** 10,765-10,772.

Manzella, G.M.R., Gasparini, G.P., Astraldi, M. (1988) Water exchange between the eastern and western Mediterranean through the Strait of Sicily. *Deep-Sea Research,* **35**, 1021-1035.

Manzella, G.M.R., Hopkins, T.S., Minnet, P.J., Nacini, E. (1990) Atlantic water in the Strait of Sicily. *Journal of Geophysical Research*, **95**, 1569-1575.

McClain, C.R., Pietrafesa, L.J., Yoder, J.A. (1984) Observations of Gulf Stream-induced and wind-driven upwelling in the Georgia bight using ocean colour and infrared imagery. *Journal of Geophysical Research,* **89**, 3705-3723.

Morel, A. (1980) In-water and remote sensing measurements of ocean colour. *Boundary Layer Meteorology,* **18**, 177-201.

Moretti, M., Sansone, E., Spezie, G., De Maio, A. (1993) Results of investigations in the Sicily channel. *Deep-Sea Research,* **40**, 1181-1192.

Onken, R., and Sellschopp, J. (1998) Seasonal variability of flow instabilities in the Strait of Sicily. *Journal of Geophysical Research, in press.*

Piccioni, A.,M. Gabriele, E. Salusti, E. Zambianchi, (1988) Wind-induced upwellings off the southern coast of Sicily, *Oceanologica*, **11**, 309-314.

Pierini, S. (1996) Topographic Rossby modes in the Strait of Sicily. *Journal of Geophysical Research,* **101**, 6429-6440.

Pietrafesa, L.J. (1983) Shelfbreak ciculation, fronts and physical oceanography:east and west coast perspectives. *Special publication, Society of Economic Paleontologists and Mineralogists,* **33**, 233-250.

Plant, W.J. (1982) A relationship between wind stress and wave slope. *Journal of Geophysical Research,* **87**, 1961-1967.

Richards, S.D., A.D. Heathershaw, N.R. Brown, and T.G. Leighton (1997) The effect of suspended particulate matter on the performance of high-frequency sonars in turbid coastal waters. *High Frequency Acoustics in Shallow Water, SACLANTCEN Conference Proceedings CP-45.*

Robinson, A.R. (1995) Physical processes, field estimation and an approach to interdisciplinary ocean modeling. *Earth-Science Reviews,* **40**, 3-54.

Robinson, A.L., Sellschopp, J., Warn-Varnas, A., Leslie, W.G., Layano, C.J., Haley, P.J., Jr. (1998) Atlantic Ionian Stream. *Journal of Marine Systems,* in press.

Rooney, D.M., and Janowitz, G.S. (1979) Flow over the Rocky and Andes mountains: applications of an analytical model. *Journal of the Atmospheric Sciences*, **36**, 549-558.

Roussenov, V., Stanev, E., Artale, V., Pinardi, N. (1995) A seasonal model of the Mediterranean Sea general circulation. *Journal of Geophysical Research,* **100**,:13515-13538.

Ryther, J.H. (1969) Upwelling. *Science*, **166**, 72-76.

Saint-Guily, B. (1982) Hydrodynamics of semi-enclosed seas. In: *Proceedings of the 13th International Liege Colloquium on Ocean Hydrodynamics*, Elsevier, pp. 155-175.

Smith, R.L. (1968) Upwelling, *Oceanogr-Mar.Biol.Ann.Rev.,* 6, 11-46.

Stoffelen, A.D., Anderson, D.L.T. (1993) ERS-1 scatterometer data characteristics and wind retrieval skill. Proceedings First ERS-1 Symposium, ESA publication Div., Noordwijk, The Netherlands, ESA SP-359.

Tziperman, E., Malanotte-Rizzoli, P. (1991) The climatological seasonal circulation of the Mediteranean Sea. *Journal of Marine Research,* **49**, 411-433.

Wackerman, C.C., Rufenach, C.L., Schuchman, R., Johannessen, J., Davidson, K. (1996) Wind vector retrieval using ERS-1 SAR imagery. *IEEE Transactions on Geoscience and Remote Sensing,* **34**, 1343-1352.

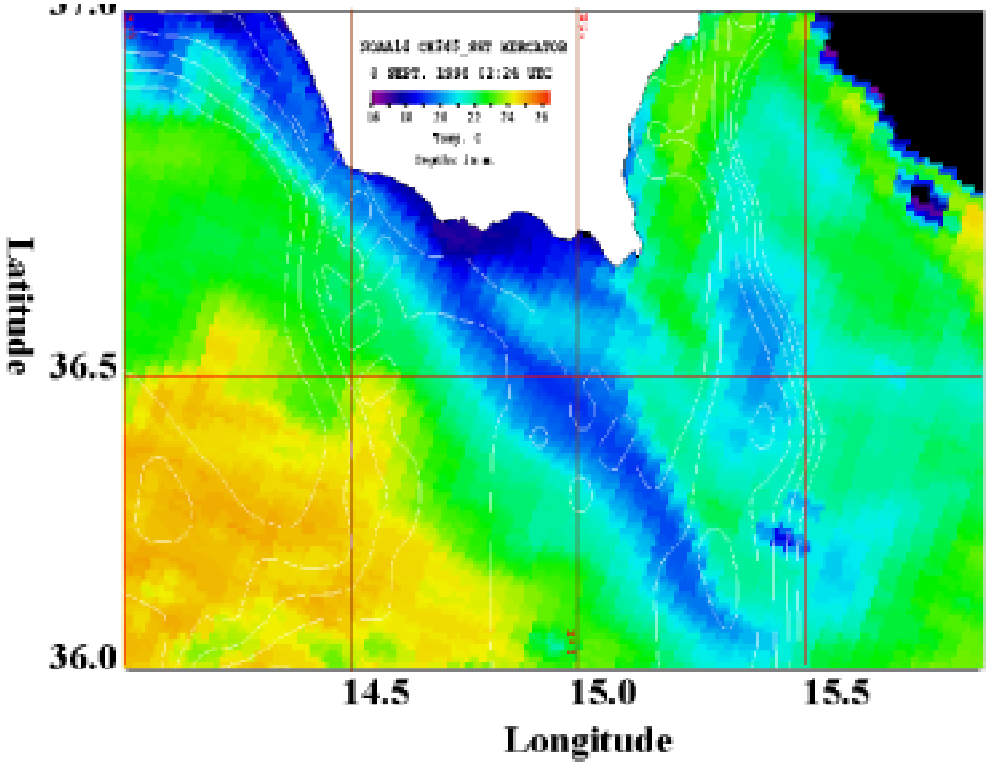

Figure 1 *The study area shown in NOAA-14 AVHRR imagery from 8 September, 1996. Upwelling regions (SST of 19 to 20C ^{0}) are evident along the coastal embayments, along a 3-5 km band running to the SE, parallel to the shelf-break and at the center of the eddy located at 36.6N,15.3E. Bathymetry contours are overlaid on the image.*

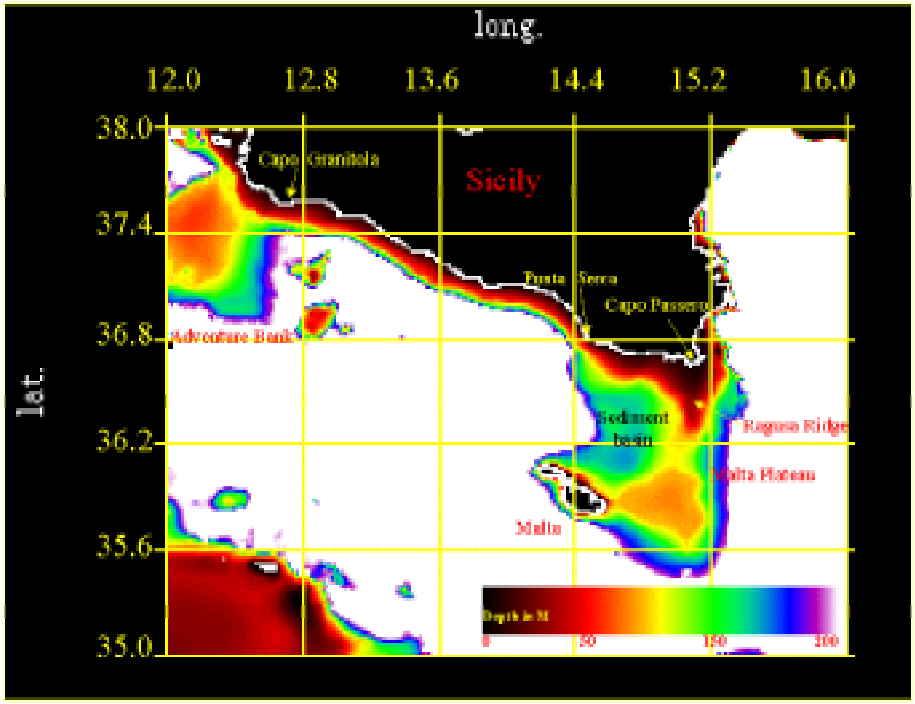

Figure 2 *Bathymetry of the region.*

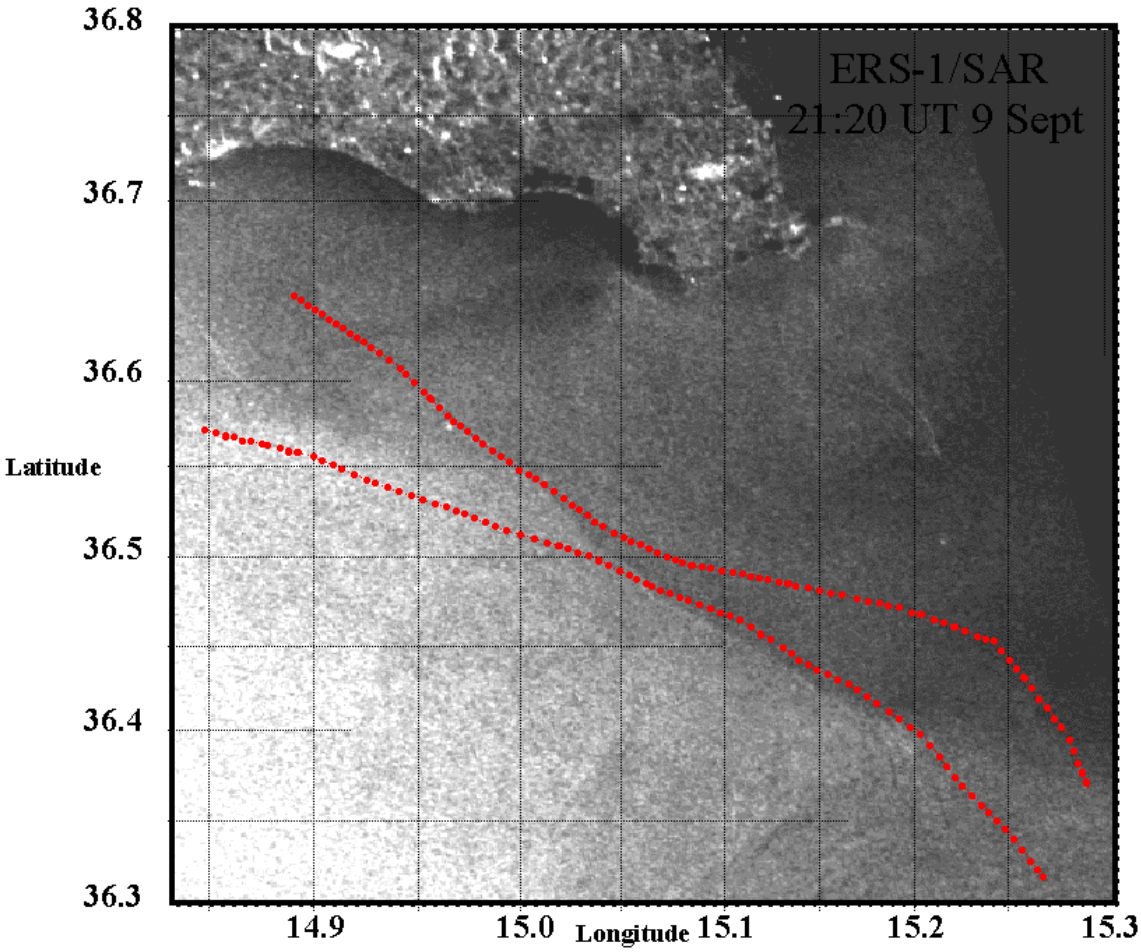

Figure 3 *ERS-2 C-band (VV-polarized) SAR image for September 9, 1996 showing step-type modulations along a diagonally oriented roughness front. The dotted lines (red) depict the boundaries of the cold filament derived from AVHRR imagery. The original image was collected in stripmap mode covering a distance of 700 km in the alongtrack direction and 100 km in the cross-track, with 150 x150 m pixel spacing.*

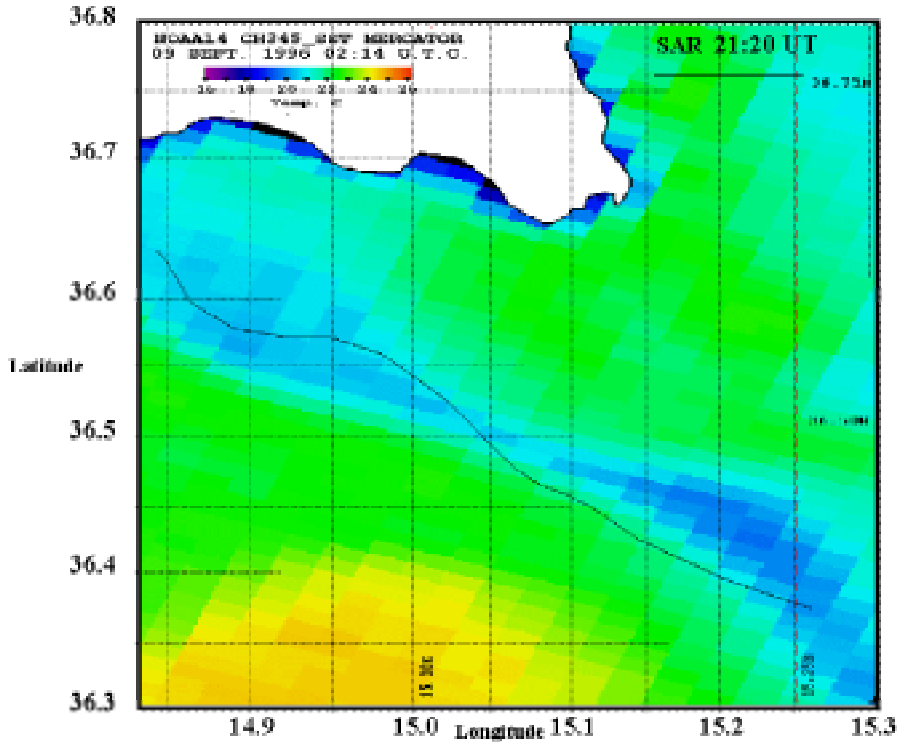

Figure 4 *NOAA-14 AVHRR imagery for 9 September, 1996 showing topographically-induced upwelling, running diagonally to the southeast. The solid line depicts the position of the roughness front.*

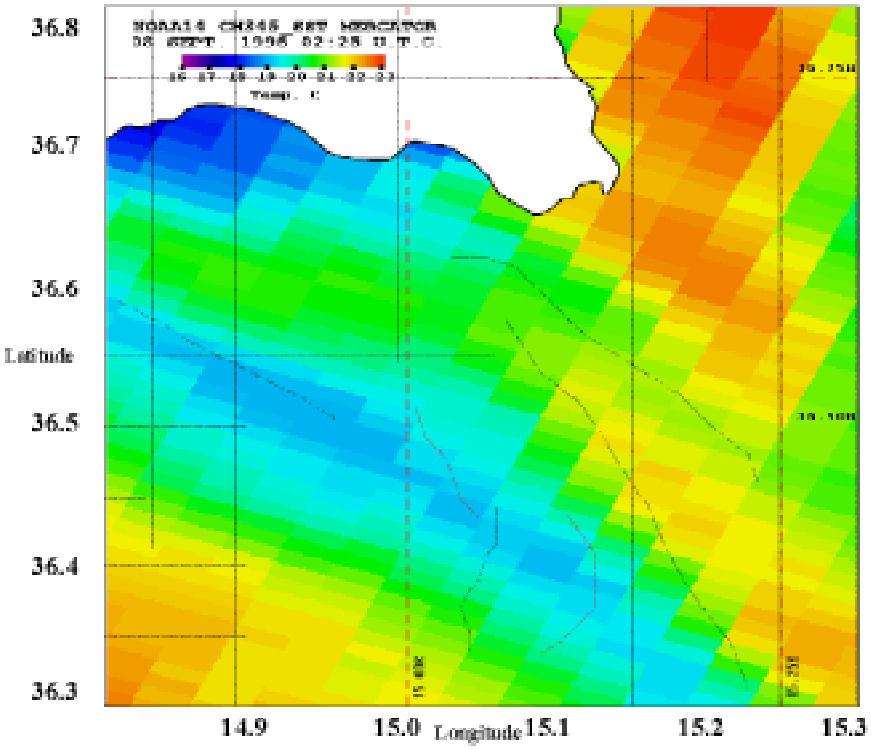

Figure 5 *Magnified image to show the region corresponding to the SAR image (Fig 6). The dotted lines depict the positions of the roughness fronts and internal wave packets appearing in Figure 6.*

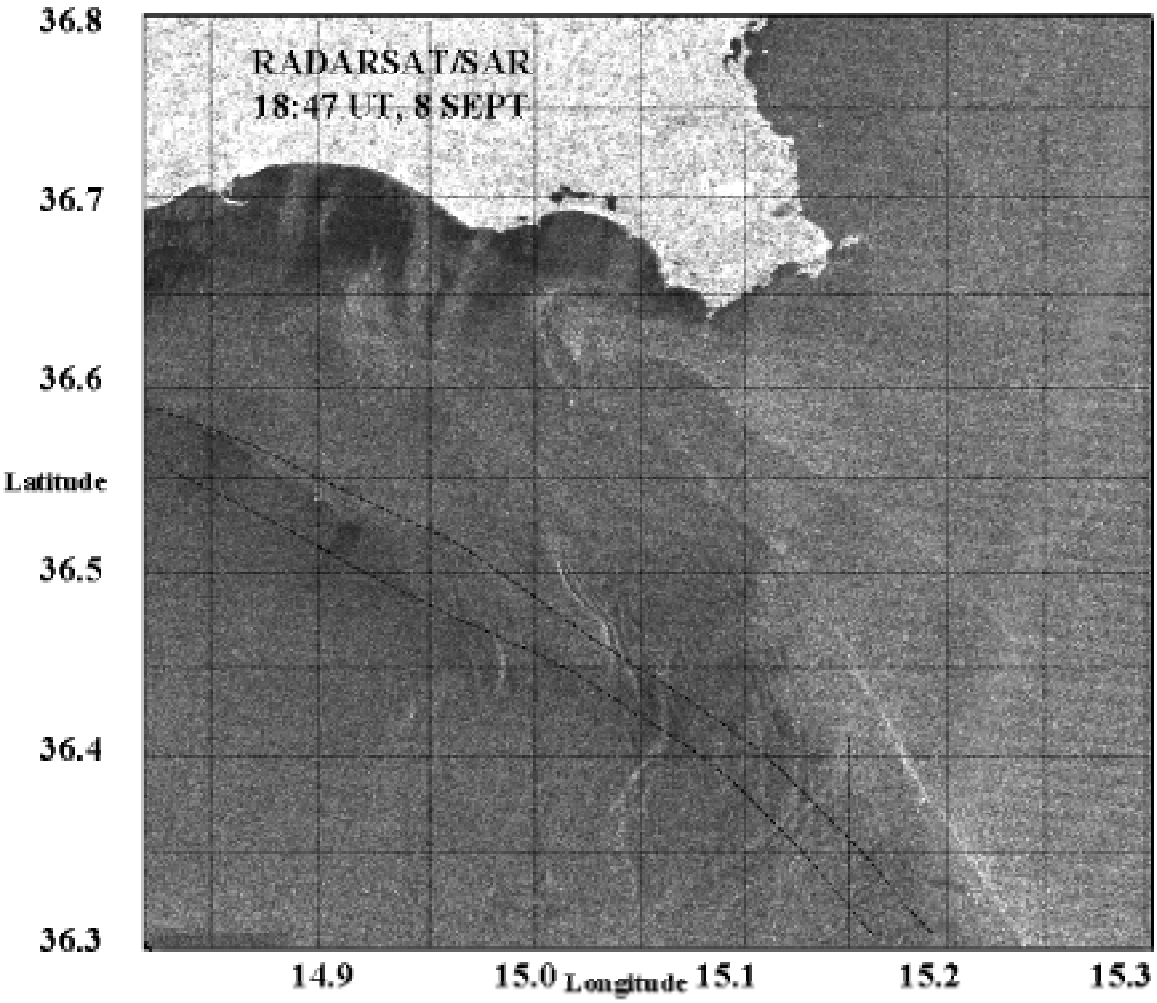

Figure 6 *RADARSAT C-band (HH-polarized) image taken on 8 September, 1996 showing regions of low radar back-scatter (along the coastal embayments), bright narrow roughness bands and internal wave packet to the southeast of Sicily . The dotted lines (red) depict the boundaries of the cold filament derived from Figure 5. The original image was collected in a SCANSAR/Narrow mode, which has a nominal swath width of 300 km and pixel spacing of 25 x 25 m. (Credit: Image collected by Radarsat International (RSI) and distributed to SACLANTCEN via DERA/Canada).*

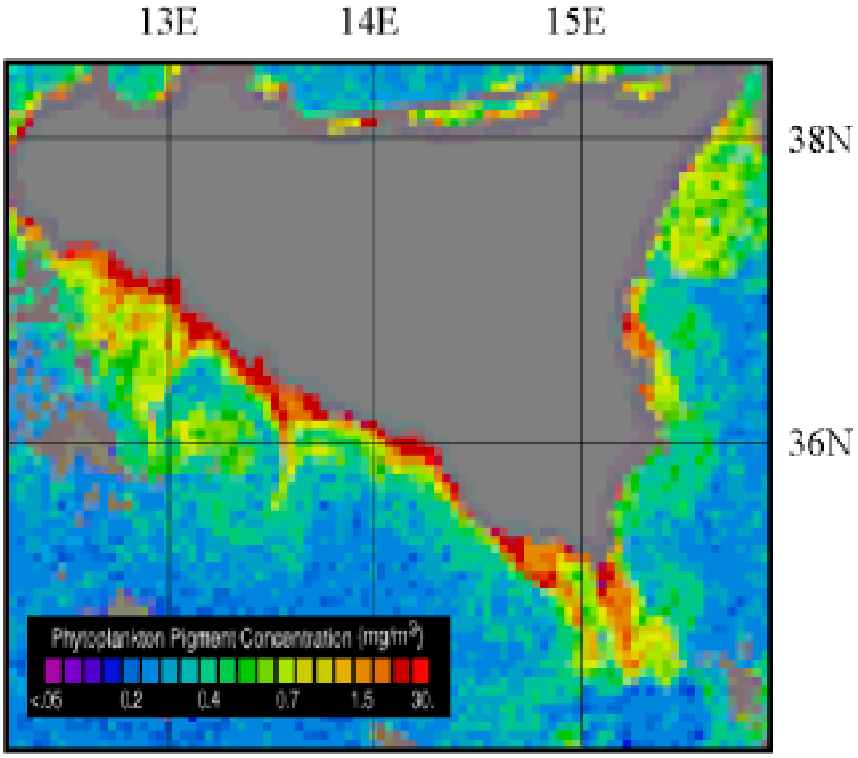

Figure 7 *CZCS image of the Strait of Sicily, 15 September 1983. Upwelling regions are characterized by high chlorophyll concentrations (red> 10 mg/m³) found along the coast, along the shelf-break, and at the center of eddies located at 37.3N, 12.8E, and 36.5N, 15.4E.*

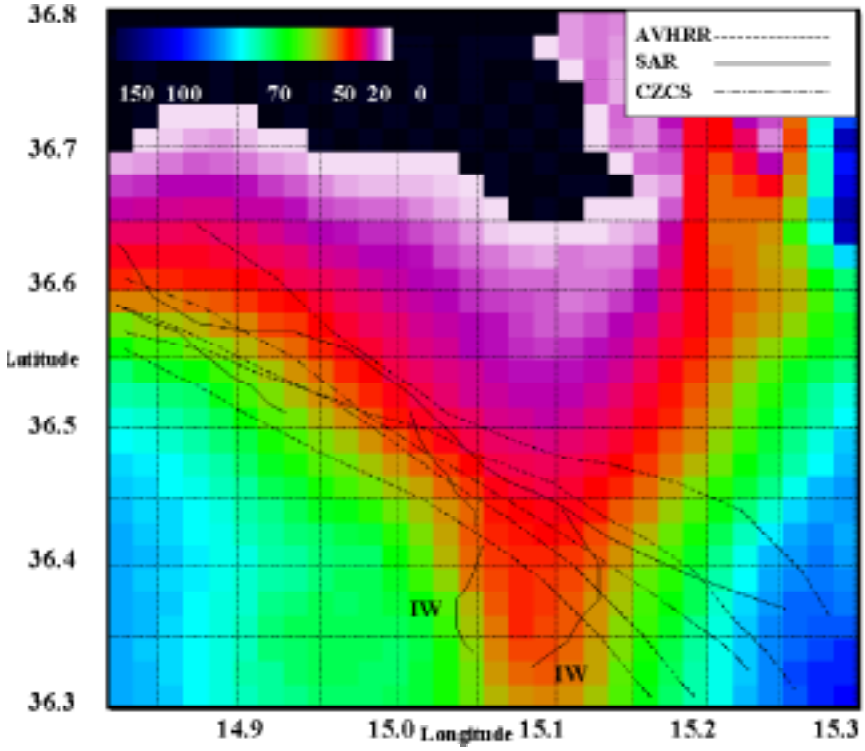

Figure 8 *Detailed bathymetry of the Malta Plateau/Ragusa Ridge. Superimposed on the map are the positions of frontal features and internal wave packets.*

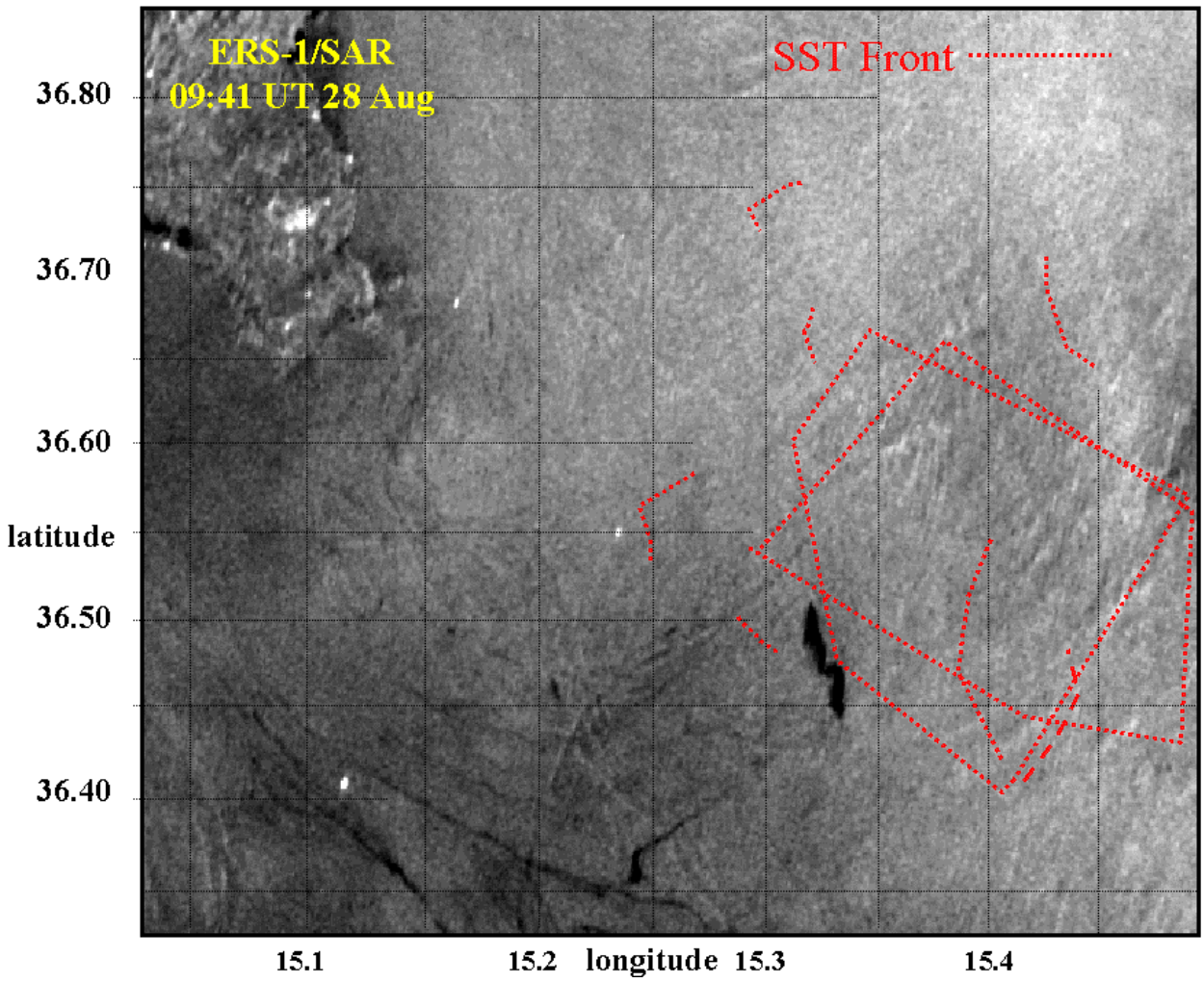

Figure 9 *ERS-1 SAR image from 28 August, 1996 showing areas of low radar back-scatter and curvilinear striations around 15.4E, 36.55N. The dotted lines (red) are the cool pool boundaries of the eddy extracted from AVHRR imagery.*

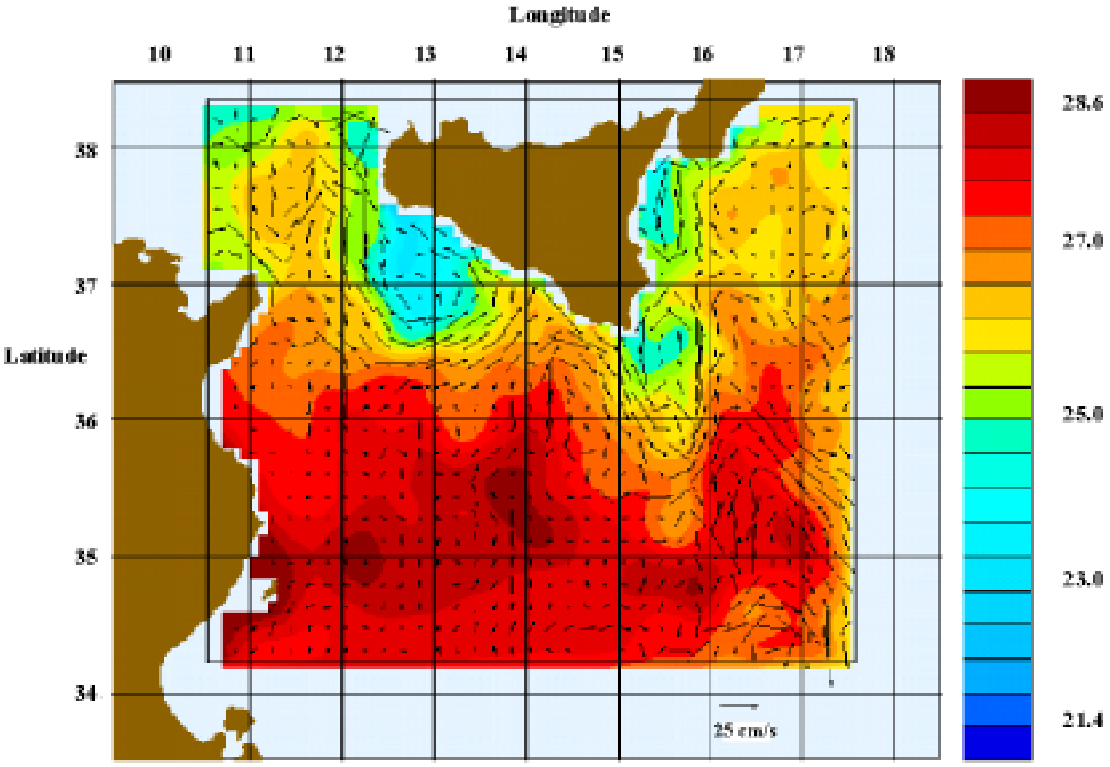

Figure 10 *HOPS SST and surface current forecast for7 September, 1996 for the Strait of Sicily. The simulation used hydrographic information from R/V Alliance as well as AXBT flights for initializing the model (from Robinson et al. 1998).*

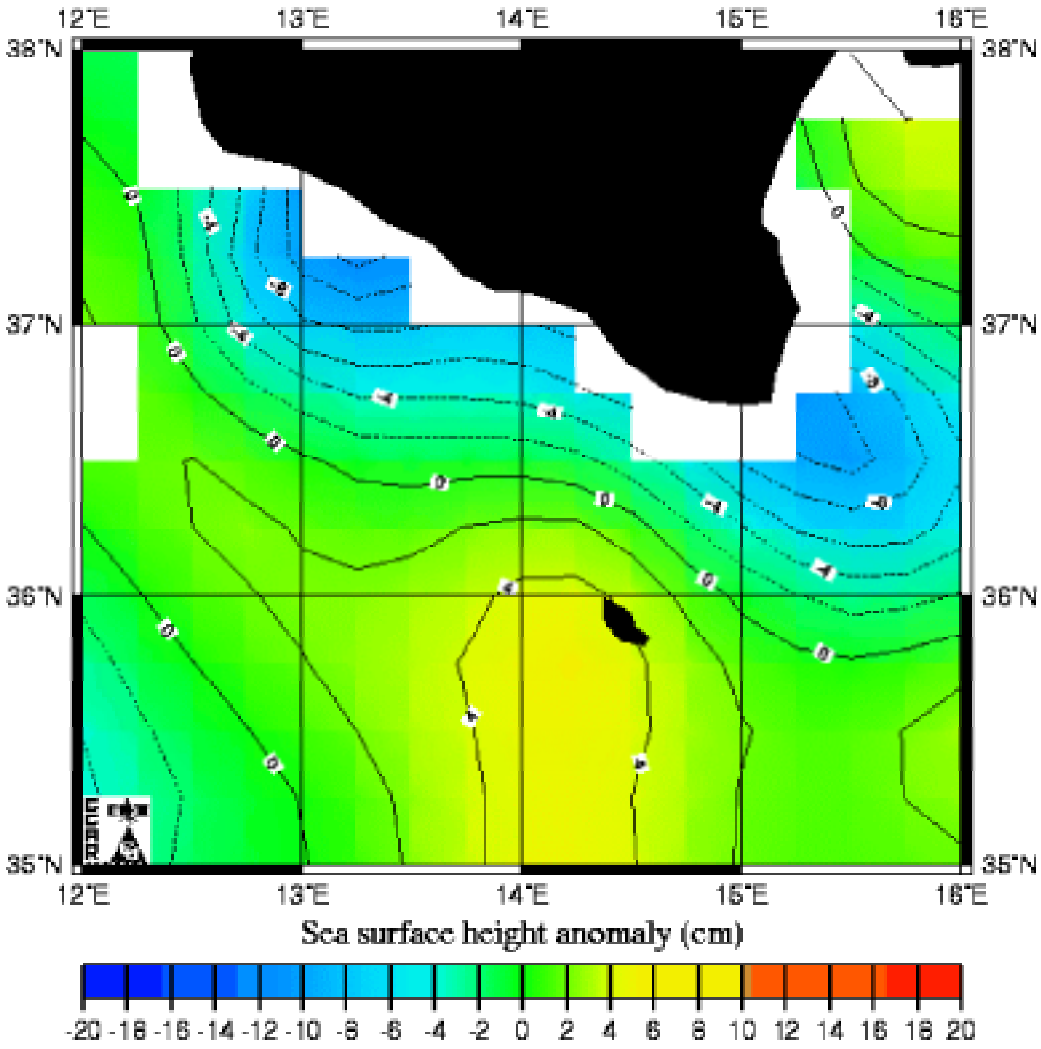

Figure 11 *Sea height anomalies derived from TOPEX/ERS-2 altimeter data for 9 September, 1996. The bowl-shaped depressions in the sea surface located at 37.4N, 13.3 E and 36.6N, 15.4E are associated with cyclonically rotating eddies appearing in the lee of Adventure Bank and the Malta Plateau.*

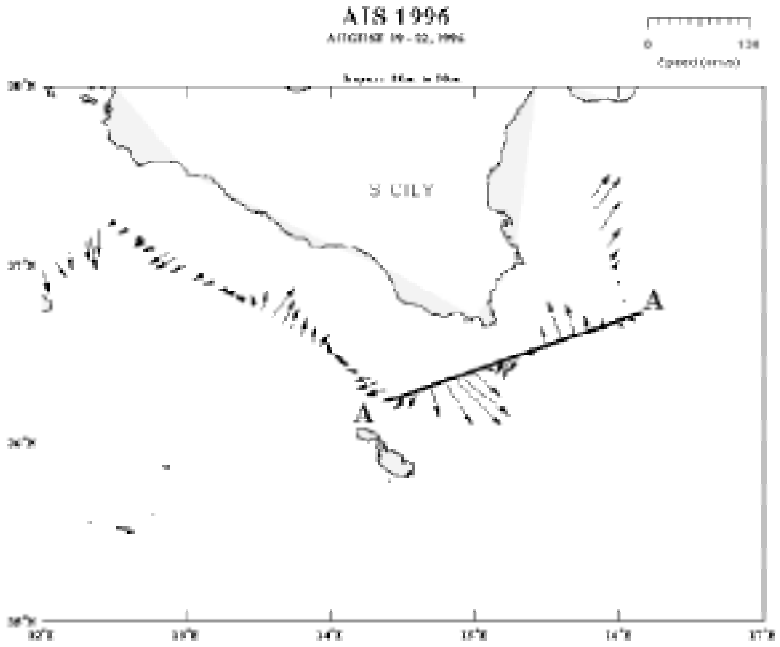

Figure 12 *ADCP measurement conducted by R/V Alliance during 19 to 22 August, 1996, show evidence of cyclonic current rotations to the southeast of the southern tip of Sicily. The currents are averaged for depths between 20 to 50 m. The solid line corresponds to location for transect A, where CTD measurements are taken.*

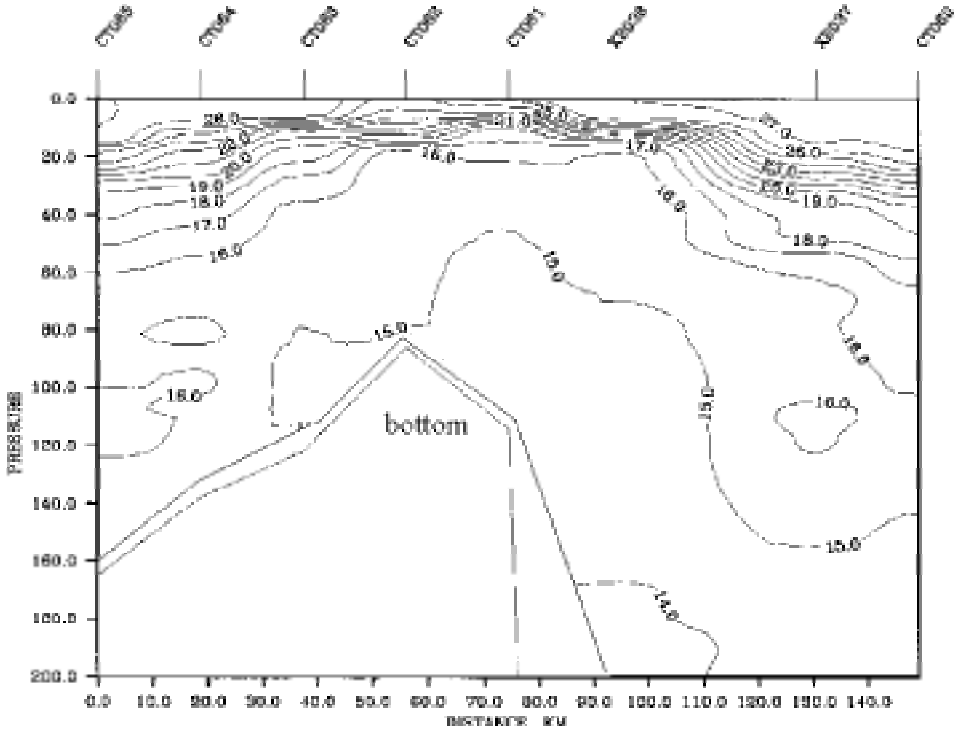

Figure 13 CTD measurements taken during 20 August 1996, along transect A showing doming of the 15°C isotherm above the shelf-break slope, and doming/squeezing of isotherms inside the cyclonically-rotating Malta eddy.

Report no. changed (Mar 2006): SR-282-UU

NATO Undersea Research Centre
Viale San Bartolomeo 400
19138 La Spezia, Italy